Front. Earth Sci. 2022, 16(2): 435–445
https://doi.org/10.1007/s11707-020-0864-7

RESEARCH ARTICLE

Karstification characteristics of the Cenomanian–Turonian Mishrif Formation in the Missan Oil Fields, southeastern Iraq, and their effects on reservoirs

Peiyuan CHEN (✉)[1], Lina GUO[1], Chen LI[2], Yi TONG[1]

1 CNOOC International Ltd., Beijing 100028, China
2 CNOOC Research Institute Co., Ltd., Beijing 100028, China

Abstract The Middle Cretaceous Mishrif Formation of the Cenomanian–Turonian age is an important Middle Eastern reservoir. Previous studies have shown that carbonates in the Mishrif Formation are affected by karstification and are concentrated at the top of the formation. However, there is a lack of systematic research on the effects of karstification on the formation's reservoir characteristics. Based on core samples, scanning electron microscopy of thin sections, and geochemical analysis of C, O, and Sr isotopes from wells in the Missan Oil Fields, unconformity was identified at the top of the B21 subzone of the Mishrif Formation. Core and cast-thin-section observations indicate that there is a significant lithological difference above and below the unconformity, and dissolution pores and voids are well-developed beneath it. Vadose silt fills the intragranular pores and geopetal fabric is developed inside some mouldic pores beneath the unconformity surface. The isotopic values of $^{87}Sr/^{86}Sr$ (0.707270–0.707722) and $\delta^{18}O$ (−5.94 ‰—−2.32 ‰) suggest that the top of the B21 subzone of the Mishrif Formation has been severely affected by syngenetic karst. Karstification is the key to high-quality reservoir formation and the reservoir's oil-bearing heterogeneity. This study will inform oil and gas exploration in the Missan Oil Fields and in other areas with similar reservoir characteristics.

Keywords unconformity, karstification, carbonate reservoir, Mishrif Formation, Missan Oil Fields, southeastern Iraq

1 Introduction

The Middle Cretaceous Mishrif Formation of the Cenomanian–Turonian age is an important rock reservoir in the Middle East (Burchette, 1993; Mahdi and Aqrawi, 2014). It is the main reservoir in oilfields such as the Buzurgan, Halfaya, Rumaila, West Qurna and Ahdab oilfields (Aqrawi et al., 1998; Sadooni, 2005; Wang et al., 2016; Liu et al., 2018; Zhong et al., 2019). The Mishrif Formation contains up to 40% of all Cretaceous oil reserves in Iraq and about 30% of all of Iraq's oil reserves (Alsharhan and Nairn, 2003).

The Mishrif Formation reservoir and similar formations have been studied in many oilfields over past decades by oil companies and individual researchers in Central and Southern Iraq, as well as elsewhere in the Middle East (Farzadi, 2006; Hollis, 2011; Hajikazemi et al., 2012; Mehmandosti et al., 2013; Vincent et al., 2015). Previous studies have shown that the carbonates in the reservoir of the Mishrif Formation were deposited in a carbonate-ramp environmental setting and were affected by karstification (Gao et al., 2013; Aqrawi et al., 1998; Wang et al., 2016; Yu et al., 2018). This karstification has been reported in several localities in Iraq and Iran, and is concentrated at the top of the Mishrif Formation (Hajikazemi et al., 2010; de Periere et al., 2017; Assadi et al., 2018); however, and there is a lack of systematic research on karstification within the Mishrif Formation. In addition, the study of karstification mostly focuses on diagenesis; there have been very few studies on karstification type and the influences of karst on reservoir properties and reservoir-development models. Observation of cores from the Missan Oil Fields of southeastern Iraq reveals many sedimentary features that reflect karstification in the Mishrif Formation.

Karstification of carbonate rocks is an important

Received June 21, 2020; accepted December 23, 2020

E-mail: swpua409@163.com

diagenetic process that contributes to the development of reservoirs by improving their porosity and permeability (Lousk, 1999; Fu et al., 2006). Karstic features have great implications for sequence stratigraphy, palaeoenvironmental interpretation and, more importantly, the development of hydrocarbon reservoirs (Jolley et al., 2010; Rahimpour-Bonab et al., 2013; Hajikazemi et al., 2010). However, the identification of these features could be problematic in some drilled cores.

The goal of this investigation is to identify karstification features in the Mishrif Formation and their influence on reservoir quality, oil-bearing differences, and reservoir-development models. To gain a better understanding of karstification, we investigated the petrography, strontium isotopes, stable carbon isotopes, and stable oxygen isotopes of Mishrif carbonates from subsurface cores in southeastern Iraq.

2 Regional geological setting

The study area is located in the Missan Province, southeastern Iraq, along the border with Iran. It is the transitional zone between the piedmont depression of Zagros and the Mesopotamian tectonic belt, which contains three oilfields — A, B, and F (Fig. 1(a)). The stratigraphy of the studied field predominantly comprises Tertiary and Cretaceous sequences. The Mishrif Formation, the focus of this study, was formed during the period from the late Cenomanian to the mid-Turonian stage, which was characterized by high sea levels (Mahdi and Aqrawi, 2014).

Regional stratigraphic and sedimentological studies (Mahdi et al., 2013; Al-Ekabi, 2015) indicate that the carbonates in the Mishrif Formation were deposited when the global sea level was high (Haq and Al-Qahtani, 2005). Following the deposition of the Mishrif Formation, a major fall in sea level during the mid-Turonian stage exposed these carbonates and resulted in a regional Turonian unconformity. Sequence stratigraphic studies of the Mishrif Formation have been constructed based on correlation of the transgressive and regressive hemicycles, which are separated by maximum flooding surfaces. One second-order sequence and three third-order sequences have been identified, which show lateral and vertical facies variations depending on relative sea-level changes (Fig. 1(b)). The Mishrif Formation has gradational contact with the underlying Rumaila Formation, and the regional unconformity at the top contacts the Khasib Formation (Fig. 1(b)). The thickness of the Mishrif Formation in the Missan Oil Fields varies between 320 m and 370 m, with an average thickness of 340 m. According to different

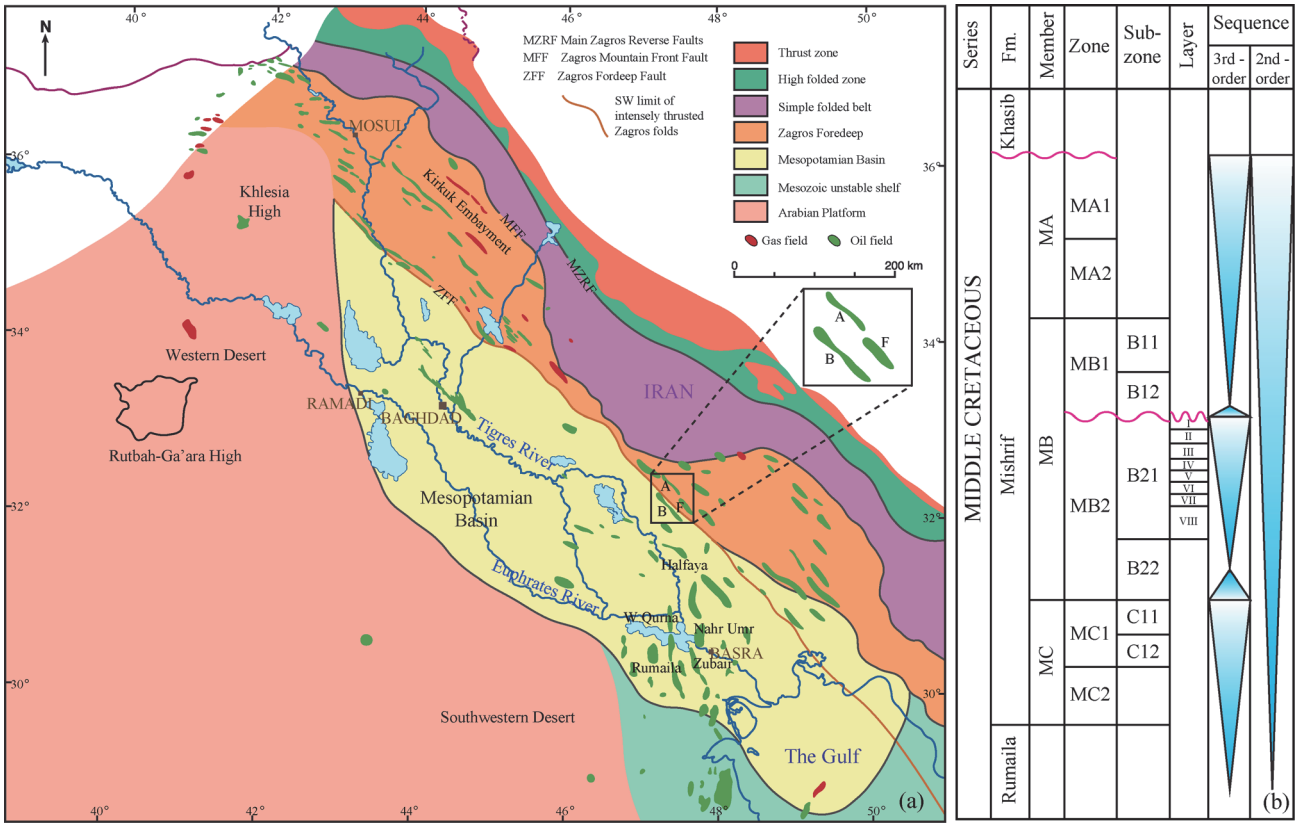

Fig. 1 (a) Regional tectonic setting of the study area (modified after Pitman et al., 2004). (b) Sequence stratigraphy and reservoir zonation of the Mishrif Formation in the Missan Oil Fields.

sedimentary, logging-curve, and petrophysical properties, the Mishrif Formation in the Missan Oil Fields can be divided into three general members, six zones, and a further six sub-zones. The B21 subzone, based on the reservoir's physical characteristics, can be further divided into eight layers from bottom to top, namely: Layer VIII, VII, VI, V, IV, III, II and I (Fig. 1(b)).

3 Materials and methods

The study was based on samples from four (sidewall) cored wells (B-51, B-52, B-22, and F-28) in the Missan Oil Fields. The total length of the cored-well sections was 172 m. The samples were prepared using a combination of petrological and geochemical methods, as introduced above. A total of 106 samples were selected for thin-section preparation, which was performed at Core Laboratories in the United Arab Emirates and the State Key Laboratory of Oil and Gas Reservoir Geology and Exploitation (Chengdu University of Technology). Thin sections were impregnated with blue resin to facilitate clear observation of the pore structure of the rock. To investigate the reservoir's porosity and permeability, 1200 horizontal core plugs from 14 wells were analysed at Core Laboratories in the United Arab Emirates.

Twenty-six samples from wells B-51, B-52 and F-28 were selected for SEM analysis (FEI-Quanta 250 FEG) and carbon (C), oxygen (O), and strontium (Sr) isotope analyses in the State Key Laboratory of Oil and Gas Reservoir Geology and Exploitation (Chengdu University of Technology). The samples for SEM were first broken up into fragments and smooth surfaces were then coated with gold to examine the mineralogy of the components, cements, textures, and pore systems. Carbon (C) and oxygen (O) stable isotopes were analysed using a mass spectrometer (MAT253). Analyses were based on the DZT0184.17-1997 standard of China. The temperature for testing was set at 35°C and the results are reported relative to the PDB standard with an analysis error of 0.01‰. Strontium isotopes were measured using a mass spectrometer (Triton Plus). Samples of approximately 70 mg were crushed and ground to 75 μm, then dissolved in 0.8 mol/L HCl in a Teflon cup. After centrifugation, the liquid was passed through an AG 50W-X8 (H^+) cation exchange column using HCl as the eluent to isolate pure strontium. For the entire process, the blank level was approximately 2×10^{-10} –5×10^{-10} and the error is expressed as $\pm2\sigma$.

4 Results

4.1 Karstification characteristics

4.1.1 Unconformity surfaces

Based on core descriptions from cored wells B-22 and F-28, unconformity surfaces were identified at the top of the B21 subzone. The strata on both sides of the interface exhibited interlocking contact, which is a direct indication of karst unconformity (Figs. 2(a) and 2(b)). The lithology changed considerably below and above the unconformity

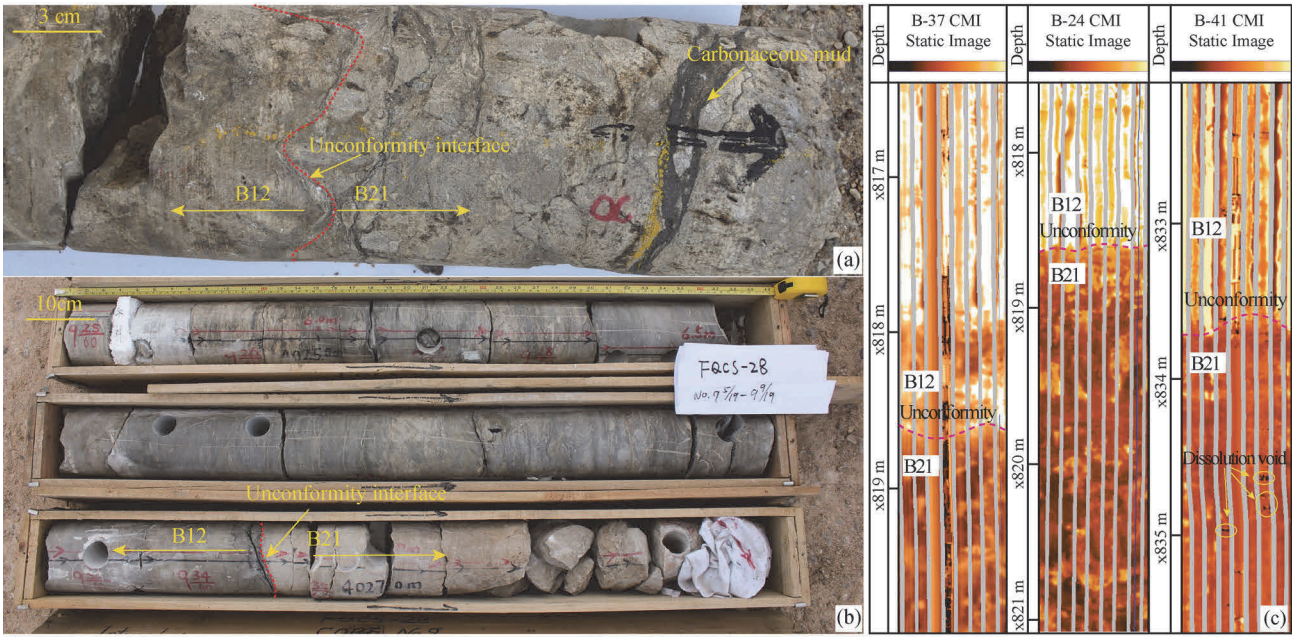

Fig. 2 Core karst unconformity features of the Mishrif Formation in the Missan Oil Fields. (a) Well B-22; (b) Well F-28; (c) Wells B-37, B-24 and B-41.

surfaces. In general, bioclast limestone with a considerable number of dissolution pores and voids developed under the unconformity surface and had good physical properties. In contrast, argillaceous limestone, a dense rock that generally cannot form effective reservoirs, was developed above the unconformity surface. Moreover, it can be seen from the imaging log (FMI) that the lithology exhibits a bright white colour above the unconformity and has a dark portion under the unconformity surface; the main contributing factor to this is dissolution (Fig. 2(c)).

4.1.2 Small dissolution voids and breccia

Core observations revealed that a number of karst identification marks were developed in the carbonate layer at the top of the B21 subzone, such as small dissolution voids and breccia. The dissolution voids were small-to-medium-sized, being 1–3 cm in width and 2–15 cm in length. The voids were partially or completely filled with coarse-grained calcite cement (Figs. 3(a) and 3(b)) and a small amount of carbonaceous mud and sand (Figs. 2(a), 3(c) and 3(d)). The small- and medium-sized voids were mostly horizontal (Fig. 3(e)) with heights of 1–2 cm, and were filled with fine-grained calcite cement. The material partially or completely fills the voids and appears to be the product of horizontal undercurrent karst zones (Luo et al. 2010; Xiao et al., 2016, 2018; Liu et al., 2019). Karst breccia is an important indicator of the presence of palaeokarst (Chen et al., 2015; Xiong et al., 2019). Cored wells in the study area exhibited the development of massive breccias in the B21 subzone. The gravel diameter was 1–10 cm and dominated by micritic limestone, and had angular or subangular shapes (Fig. 3(f)).

With increasing depth, the size of the dissolution voids decreased from the centimetre to millimetre scale and gradually decreased in number (Fig. 4).

4.1.3 Microscopic features

Examination of core thin sections by polarized-light microscopy indicates that dissolution and mouldic pores developed in the bioclastic limestone under the unconformity (Figs. 5(a)–5(c)), and that suspended cement developed between the particles (Fig. 5(d)). Vadose silt developed in the intragranular pores to form a special geopetal fabric (Fig. 5(e)). The geopetal fabric developed inside some mouldic pores beneath the unconformity surface (Figs. 5(e) and 5(f)). These observations, in conjunction with the core observations, indicate the presence of karstification (Xiao, 2017).

4.2 Geochemistry

4.2.1 C and O isotopes

C and O isotope analyses were performed on Wells B-51, B-52, and F-28 in the B21 subzone. The $\delta^{18}O$ and $\delta^{13}C$ values were obtained from calcitic matrices. The $\delta^{13}C$

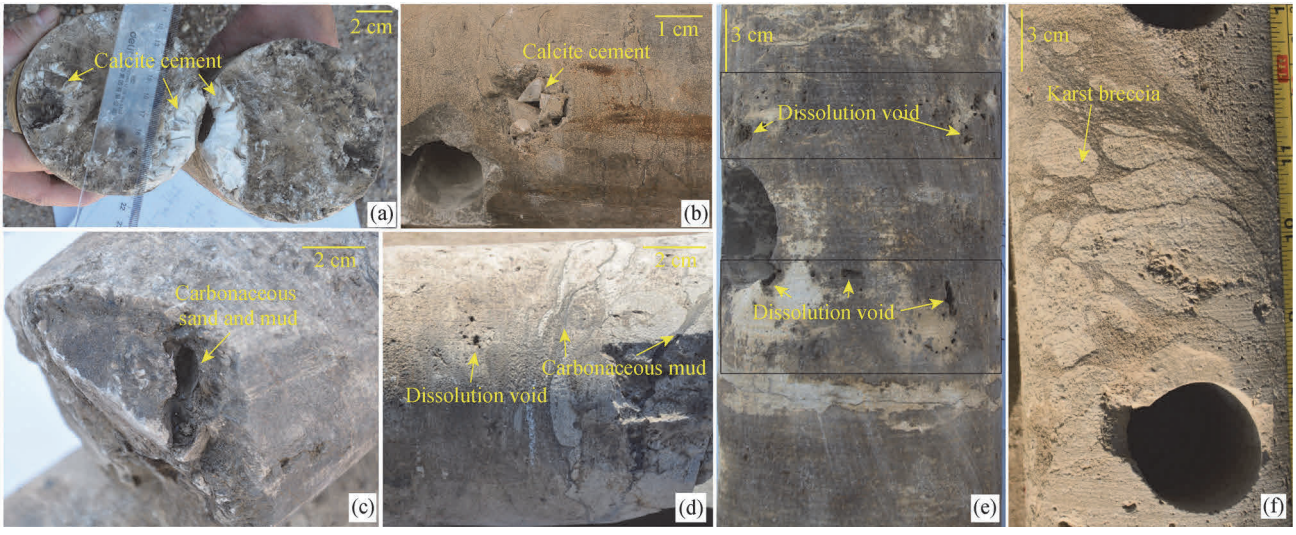

Fig. 3 Core-based identification of dissolved voids in the Mishrif Formation. (a) Well B-22 at x916.3 m (B21 subzone), exhibiting the existence of bioclastic limestone and development of karst voids filled with calcite cement; (b) Well F-28 at x111.4 m (B21 subzone), exhibiting the presence of packstone and development of voids filled with calcite cement; (c) Well B-22 at x913.5 m (B21 subzone), exhibiting the presence of bioclastic limestone with development of karst voids and dissolved voids filled with carbonaceous sand and mud; (d) Well B-22 at x914.5 m (B21 subzone), exhibiting the presence of bioclastic limestone with development of karst voids and dissolved voids filled with carbonaceous mud; (e) Well B-22 at x916.5 m (B21 subzone), exhibiting the presence of bioclastic limestone and development of mostly horizontal unfilled voids; and (f) Well B-22 at x921.4 m (B21 subzone), exhibiting the presence of bioclastic limestone and development of karst breccia.

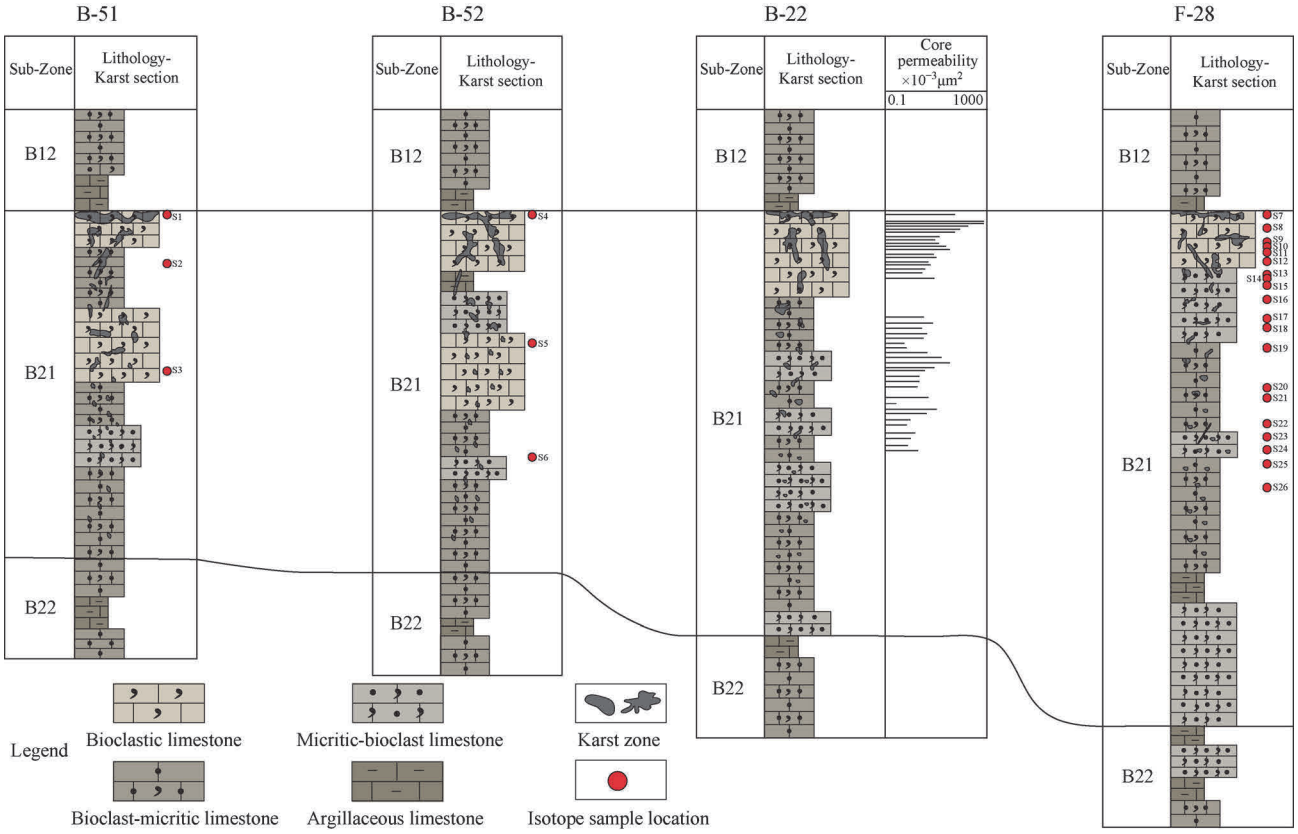

Fig. 4 Correlation profile of karstification in the B21 subzone.

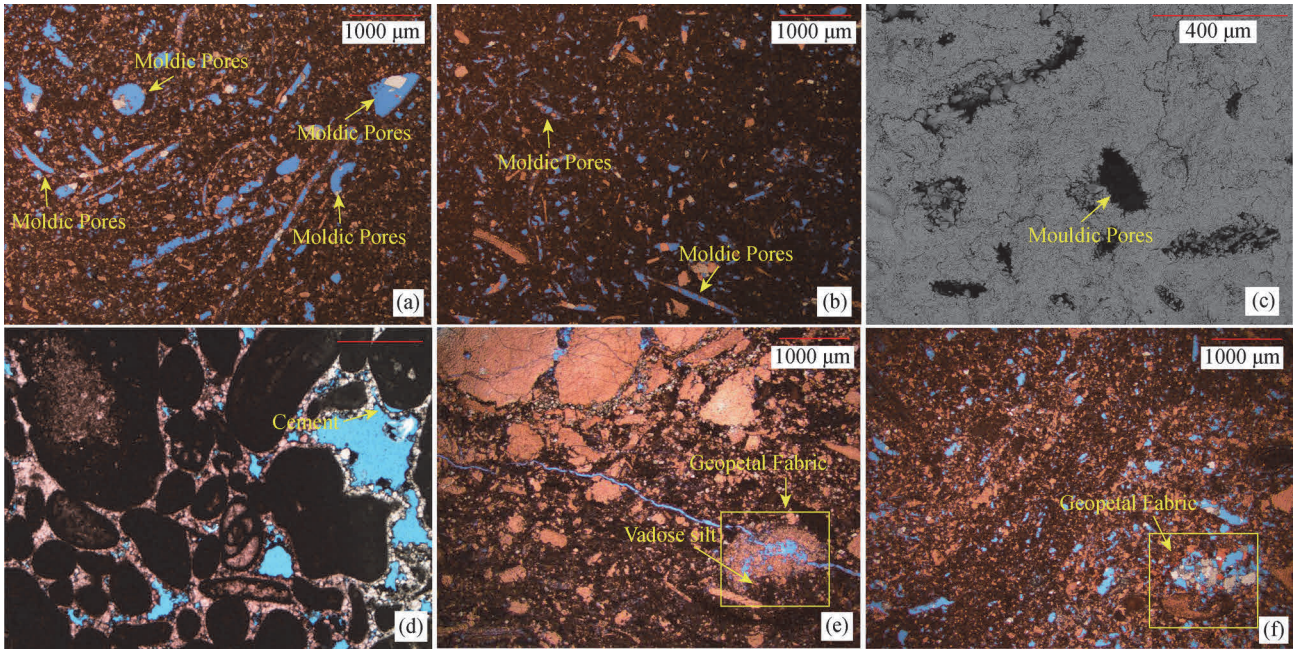

Fig. 5 Micrographs of the Mishrif Formation. (a) Well B-22 at x943.1 m (B21 subzone), exhibiting the presence of packstone with predominantly secondary mouldic pores; (b) Well B-22 at x957.2 m (B21 subzone), exhibiting the presence of packstone and development of mouldic pores; (c) Well F-28 at x087.7 m (B21 subzone), exhibiting the presence of packstone with mouldic pores (SEM); (d) Well B-52 at x907.0 m (B21 subzone), exhibiting the presence of grainstone with primary intergranular pores and development of cement (the arrow indicates suspended cement); (e) Well B-22 at x941.1 m (B21 subzone), exhibiting the presence of packstone with secondary dissolution, mouldic pores and microporosity, along with development of geopetal structures; and (f) Well B-22 at x942.2 m (B21 subzone), exhibiting the presence of skeletal peloidal packstone with echinoderms and the development of geopetal structures.

values generally ranged between 2.31‰ and 3.49‰ with an average of 2.95‰. The $\delta^{18}O$ values were generally distributed in the range of −5.94‰—−2.32‰ with an average of −5.00‰ (Fig. 6(a)).

4.2.2 Sr isotopes

The $^{87}Sr/^{86}Sr$ ratios for limestone in the B21 subzone of the Mishrif Formation are shown in Fig. 6(b). They were generally distributed between 0.707270 and 0.707722 (average = 0.707476) and clearly did not vary significantly.

5 Discussion

5.1 Karstification type

Karstification can occur at various diagenetic stages, including the meteoric and deep burial stages, and in mixed zones (Xiao et al., 2019b; Jia et al., 2016; Cazarin et al., 2019). The type of karstification in the study area is syngenetic karst, based on the presence of the unconformity surface, pore and void systems, the nature of the fillings, and geochemical characteristics.

Syngenetic karst, also known as syn-depositional karst, refers to the selective fabric dissolution of susceptible minerals in meteoric water during short-term exposure as a result of syn-sedimentary sea-level change and rapid sediment deposition (James and Choquette, 1988; Xiao et al., 2019a). This karstification has typical identification marks, such as selective dissolution, vadose silt, geopetal structures (Scholle and Ulmer-Scholle, 2003; Moore and Wade, 2013), small dissolution voids, breccia and suspended cement (Xiao, 2017). These characteristics were identified in this study; thus, we conclude that the karstification in the study area is syngenetic karst.

The Mishrif Formation has developed selective dissolution pores and voids, such as mouldic pores. This indicates that the strata had been exposed to a meteoric-water environment in which they experienced leaching or dissolution by a mixture of meteoric water and seawater that caused the selective formation of intragranular dissolution pores (Chen et al., 2015). Suspended cement often forms in the freshwater seepage zone and fills in intergranular pores with water and air under the influence of gravity (Xiao, 2017). Vadose silt became concentrated in the vadose zone during early exposure to the vadose diagenetic environment, suggesting syngenetic karstification (Qiang, 1998; Scholle and Ulmer-Scholle, 2003). The geopetal fabric also indicates that the strata have been exposed to a meteoric water environment (Xiao et al, 2019a, 2019b; Zhong et al., 2019). In general, the dissolution of pores and voids occurred at a small scale, and there was no mud loss in any of the wells during drilling. This is related to the limited dissolution scale of karstification itself, and syngenetic karst has these typical characteristics. All of these observations support the interpretation of syngenetic karstification.

Additionally, in terms of geochemistry, the $\delta^{13}C$ values of Cenomanian–Turonian seawater are generally 0‰—3.5‰, while the $\delta^{18}O$ values are −0.2‰—−4‰ (Veizer et al, 1999). The C isotope values in the study area ($\delta^{13}C$: 2.31‰—3.49‰) indicate that it contains similar seawater; however, the $\delta^{18}O$ values of −5.94‰—−2.32‰ are lower than those of seawater. This can be related to a gradual decrease in salinity, increasing temperatures of diagenetic fluids (Machel and Lonnee, 2002), or the influx of freshwater (Roberts et al., 2018). The climate in the Cenomanian–Turonian stage was generally warm and humid (Aqrawi et al., 1998; Rahimpour-Bonab et al., 2012). The *Z*-values (where $Z = 2.048 (\delta^{13}C\ PDB + 50) + 0.498 (\delta^{18}O\ PDB + 50)$) of all samples were higher than 120, so the low O-isotope value has an insignificant relationship with the decrease in salinity. Furthermore, it can be seen from Fig. 7(b) that all the $^{87}Sr/^{86}Sr$ ratios in the B21 subzone are within the range of that of seawater in the Cenomanian–Turonian period (0.707250–0.707736; Veizer et al., 1999), without the feature of negative bias. The major causes for the fluctuations in seawater $^{87}Sr/^{86}Sr$ ratios are the relative fluxes from two strontium sources with dissimilar isotope ratios. These are 1) the riverine flux of radiogenic strontium from continental silicate weathering

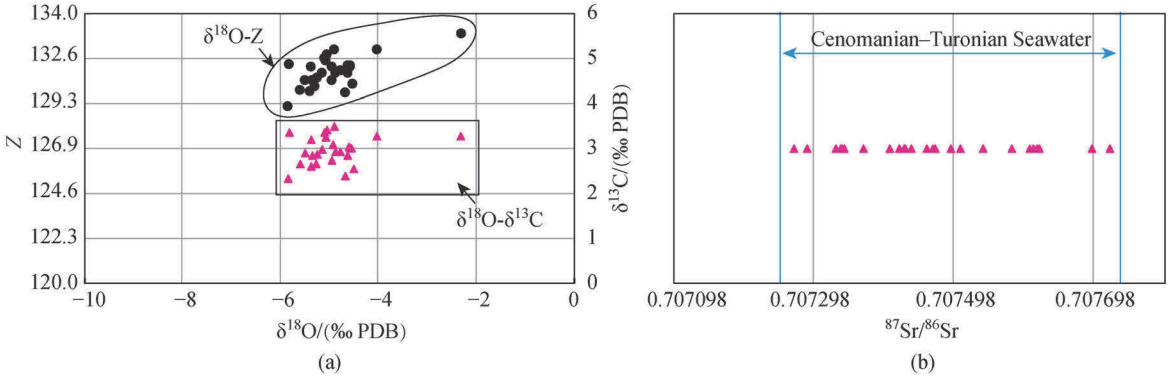

Fig. 6 (a) Carbon and oxygen isotopic variation and (b) strontium isotopic variation of carbonates in the Mishrif Formation.

(high $^{87}Sr/^{86}Sr$ ratios, average of 0.7119) and 2) the flux of low-radiogenic 'mantle' strontium from hydrothermal circulation in mid-oceanic ridges (low $^{87}Sr/^{86}Sr$ ratios, average of 0.7035; Palmer and Edmond, 1989; Taylor and Lasaga, 1999). Further, the low O isotope value indicates that the limestone was not affected by hydrothermal action. This is probably due to the transformation of atmospheric freshwater near the surface or the relatively short exposure caused by frequent fluctuations in sea level during the deposition process.

All of the above petrographic and isotopic characteristics indicate that syngenetic karst took place in the study area in the B21 subzone.

5.2 Impacts of syngenetic karstification

5.2.1 Impact on reservoir formation

Karstification is an important form of constructive diagenesis that improves the porosity and permeability of carbonate reservoirs (Choquette and James 1988; Hopkins 1999). As mentioned previously, the reservoir in this study experienced syngenetic karstification at the top of the B21 subzone. The bioclast shoal reservoir in the B21 subzone was deposited in a regressive sedimentary sequence associated with a temporary decline in sea level, so the sediments were exposed to a freshwater environment. As it was exposed to a humid and rainy climate, leaching and dissolution by atmospheric freshwater rich in CO_2 led to dissolution and the formation of various pores and karst voids of different sizes and shapes. This is the predominant reason for the formation of high-quality reservoirs in the study area.

Based on statistical analysis of the core physical properties of different layers of the B21 subzone affected by karstification, it was found that reservoir's porosity varied only slightly, while its permeability gradually deteriorated from layer I (top) to layer VIII (bottom; Fig. 7). This inverse permeability characteristic is mainly due to the fact that the dissolution intensity of dissolving water decreases with depth. Improvement of the pore-throat structure caused by syngenetic karstification is the primary reason for the permeability difference observed in the reservoir. Such inverse permeability is advantageous for the downward movement of water and upward movement of oil, and is affected by differences in density and capillary force.

5.2.2 Impact on reservoir connectivity

In the B21 subzone, the reservoir is dominated by pores and micro-fractures are uncommon (Chen, 2019). Influenced by the vertical distribution of high-quality reservoirs, all the perforation intervals of producers are located at the top of the B21 subzone; however, the pressure depletion from top to bottom is consistent (Fig. 8), which

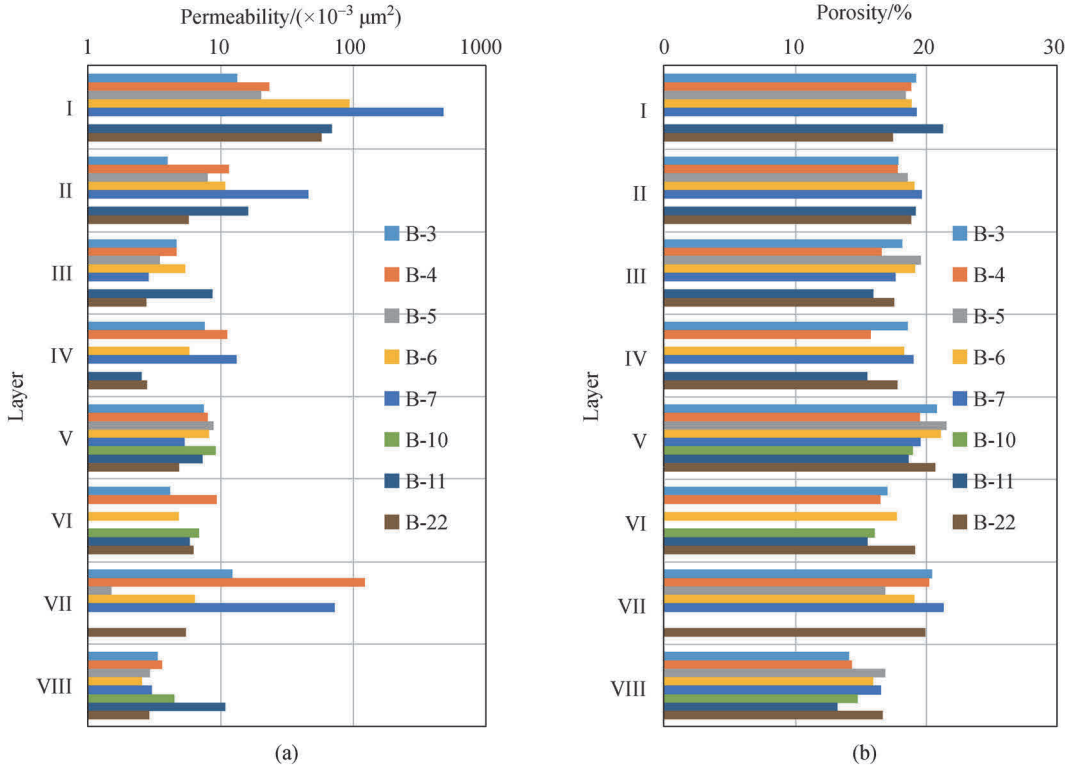

Fig. 7 Comparison of the (a) porosity and (b) permeability of different layers in the B21 subzone according to core samples.

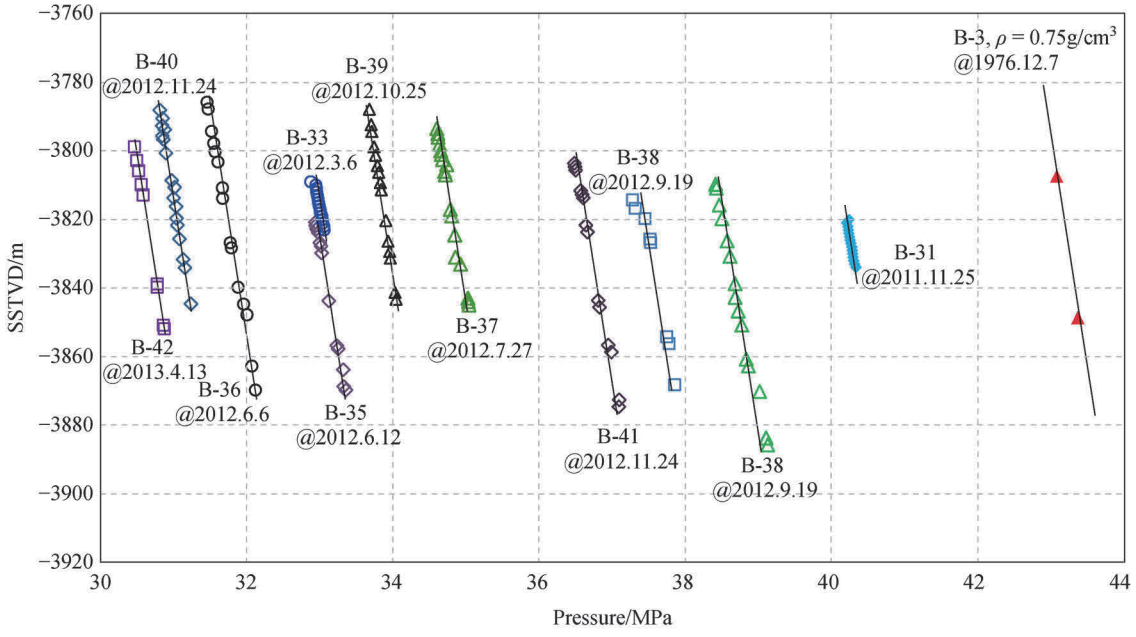

Fig. 8 Formation pressure scatterplot of a single well in the B21 subzone.

indicates that the reservoir has good vertical connectivity.

Core observations show that, with increasing depth, the number of dissolution pores and voids decreases, while those in the middle and lower parts of the B21 subzone manifest with 'piebald' features (Fig. 9). 'Piebald' karst systems are also referred to as 'sponge-like' (Baceta et al., 2007). Owing to the meteoric water karstification origin of the 'piebald' system, the underground water should form a

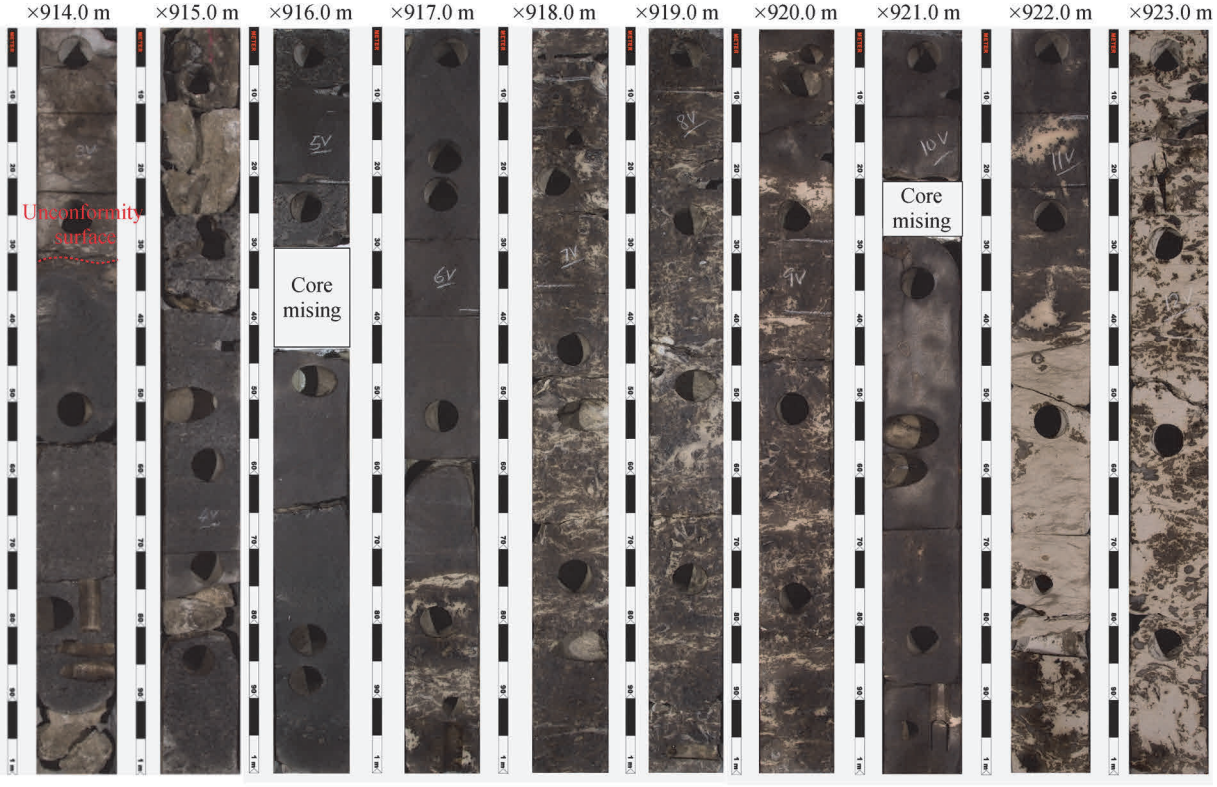

Note: Black color means the dissolution pores/voids filled with residual oil.

Fig. 9 Core slabs showing a decrease in the dissolution of pores and voids with depth (Well B-22).

well-connected system; therefore, the many 'piebald' patches formed by the water should be connected on a larger scale. However, because the pores are in patches in the rock, the 'piebald' system in the small-core samples exhibited strong anisotropy (Jin et al., 2014). Further analysis indicates that the 'piebald' voids and pores were connected to each other in the Mishrif Formation (Fig. 10). This characteristic of the reservoir facilitates the longitudinal transmission of pressure and can effectively improve the oil-sweep efficiency of bottom-injection and top-production extraction modes.

5.2.3 Impact on the oil-bearing difference

Further analysis shows that the 'piebald' pores and voids have a significant effect on the oil-bearing difference in reservoirs. According to the frequency of karst zone occurrence at core sample points with different oil-bearing grades (Fig. 11(a)), in oil-saturated and oil-rich cores, strong karst zones are dominant (74% occurrence frequency), followed by 'piebald' karst zones (26%). In the oil-immersed grade, the occurrence frequencies are 22% strong karst zones, 76% 'piebald' karst zones and 2% tight basement zones. In the oil-spot grade, the occurrence frequencies are 4% strong karst zones, 61% 'piebald' zones and 35% tight basement zones. In the oil-trace grade, the frequencies are 85% tight basement zones and 15% 'piebald' zones, with no strong karst zones.

Coring interval data from different karst zones demonstrate that the strong karst zone has the best physical properties (average porosity = 18.9%, permeability = 58.2 $\times$ 10^{-3}μm^2), followed by the 'piebald' karst zone (average porosity = 16.6%, permeability = 6.7 $\times$ 10^{-3} μm^2; note that, according to Fig. (9), the permeability of the 'piebald' karst zone may be much higher). The tight basement zone has the worst physical properties, with an average porosity of 6.3% and permeability of 2.1 $\times$ 10^{-3}μm^2. It can be seen that the oil-bearing grade has obvious karstification-controlled characteristics at the macroscopic scale. As the depth increases, the oil-bearing grading gradually changes from oil-rich and oil-immersed to oil-spot and oil-trace. Further, from the perspective of the oil-bearing grades, relatively oil-rich sections present higher karst development intensities at the top of the B21 subzone, and the wells develop voids and have better physical properties (Fig. 7). This is the main reason why all the producers are perforated at the top of the B21 subzone.

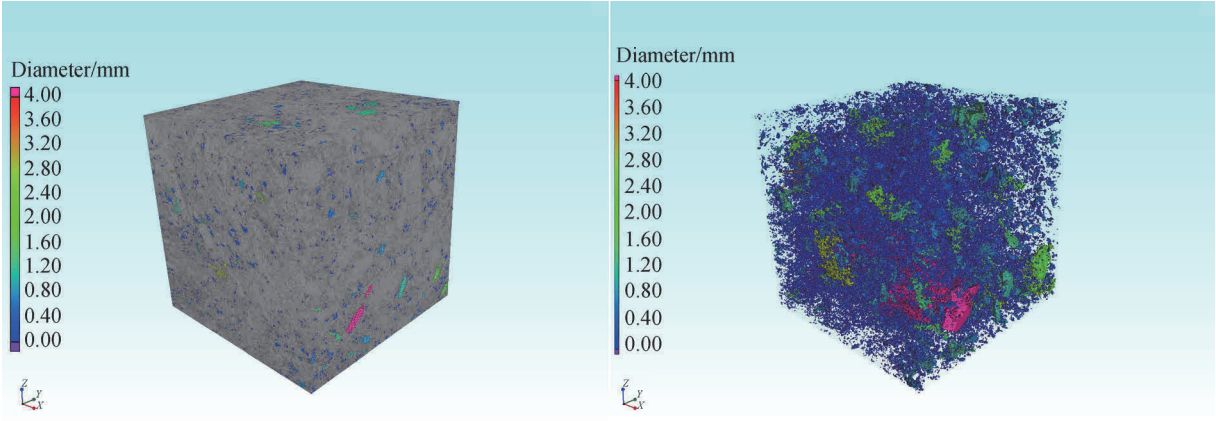

Fig. 10 (a) Three-dimensional digital rock model and (b) pore network model.

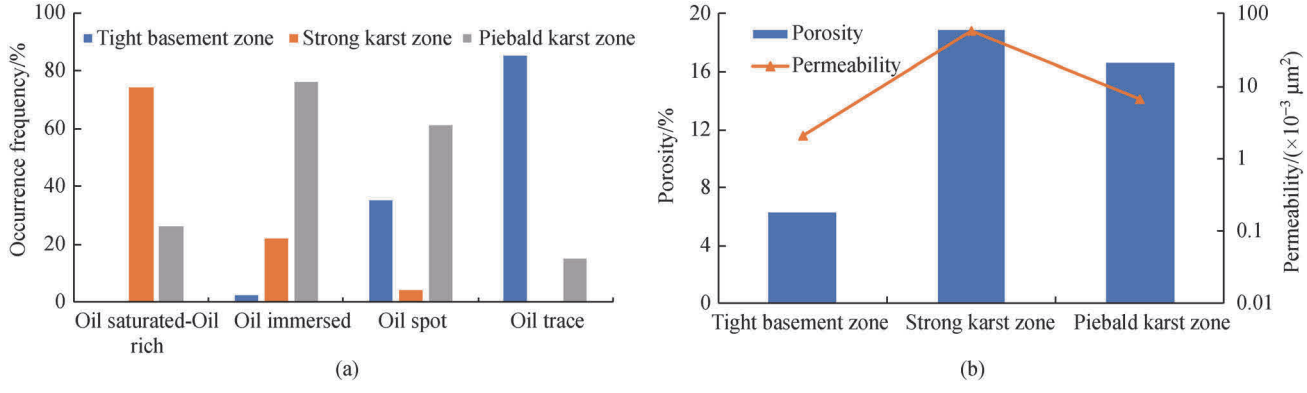

Fig. 11 (a) Frequency of karst zone occurrence in different oil-bearing grades and (b) physical properties of different karst zones.

6 Conclusions

By combining detailed core examinations with cast thin-section and geochemical analyses, several conclusions can be drawn, as listed below.

1) Based on core and FMI data from the Missan Oil Fields, an unconformity surface was identified at the top of the B21 subzone of the Mishrif Formation. Karstification is the main cause of the unconformity between the weathering surfaces at the top of the B21 subzone. Karstification is associated with the formation of dissolution features such as selective dissolution, breccia, vadose silt, geopetal structures and suspended cement.

2) Analysis of the macroscopic and microscopic characteristics of karstification and the characteristics of carbon, oxygen, and strontium isotopes indicates that the type of karstification in the study area is syngenetic karstification.

3) Syngenetic karstification resulted in increases in porosity and permeability, and affected the reservoir's vertical connectivity and oil-bearing heterogeneity. The high-quality reservoirs located at the top of the B21 subzone exhibit higher karst development intensity. The karst intensity decreases with depth, as do the reservoir's physical properties. This also affects the oil grade, which changes from oil-rich and oil-immersed to oil-spot and oil-trace.

Acknowledgements We thank anonymous reviewers for detailed and constructive feedback that helped improve the manuscript. This work was supported by the Chinese "13th Five-year Plan" National Science and Technology Major Project (No. 2017ZX05032004-001).

References

Al-Ekabi A H S (2015). Microfacies and environmental study of the Mishrif Formation in Noor field. Arab J Geosci, 8(8): 5779–5794

Alsharhan A S, Nairn A E M (2003). Sedimentary Basins and Petroleum Geology of the Middle East. Amsterdam: Elservier

Aqrawi A A M, Thehni G A, Sherwani G H, Kareem B M A (1998). Mid-Cretaceous rudist-bearing carbonates of the Mishrif Formation: an important reservoir sequence in the Mesopotamian basin, Iraq. J Pet Geol, 21(1): 57–82

Assadi A, Honarmand J, Moallemi S A, Abdollahie-Fard I (2018). An integrated approach for identification and characterization of palaeo-exposure surfaces in the upper Sarvak formation of Abadan plain, SW Iran. J Afr Earth Sci, 145: 32–48

Baceta J I, Wright V P, Beavington-Penney S J, Pujalte V (2007). Palaeohydrogeological control of palaeokarst macro-porosity genesis during a major sea-level lowstand: Danian of the Urbasa-Andia plateau, Navarra, North Spain. Sediment Geol, 199(3–4): 141–169

Burchette T P (1993). Mishrif Formation (Cenomanian-Turonian), southern Arabian Gulf: carbonate platform growth along a cratonic basin margin. In: Simo J A, Scott RW, Masse J-P, eds., Cretaceous Carbonate Platforms. AAPG Memoir. 56: 185–199

Cazarin C L, Bezerra F H R, Borghi L, Santos R V, Favoreto J, Brod J A, Auler A S, Srivastava N K (2019). The conduit-seal system of hypogene karst in neoproterozoic carbonates in northeastern Brazil. Mar Pet Geol, 101: 90–107

Chen P Y, Tan X C, Yang H T, Tang M, Jiang Y W, Jin X J, Yu Y (2015). Characteristics and genesis of the Feixianguan Formation oolitic shoal reservoir, Puguang gas field, Sichuan Basin, China. Front Earth Sci, 9(1): 26–39

Chen P Y (2019). Characteristics of micro-fractures in carbonate reservoir of Mishrif Formation, B Oilfield of Iraq. Journal of Northeast Petroleum University, 43(6): 62–72 (in Chinese)

Choquette P W, James N P (1988). Palaeokarst. New York: Springer

Farzadi P (2006). The development of Middle Cretaceous carbonate platforms, Persian Gulf, Iran: constraints from seismic stratigraphy, well and biostratigraphy. Petrol Geosci, 12(1): 59–68

Fu Q, Qing H, Bergman C M (2006). Paleokarst in Middle Devonian Winnipegosis mud mounds, subsurface of south-central Saskatchewan, Canada. Bull Can Pet Geol, 54(1): 22–36

Gao J X, Tian C B, Zhang W M, Song X M, Liu B (2013). Characteristics and genesis of carbonate reservoir of the Mishrif Formation in the Rumaila oil field, Iraq. Acta Petrol Sin, 34(10): 843–852

Hajikazemi E, Al-Aasm I S, Coniglio M (2010). Subaerial exposure and meteoric diagenesis of the cenomanian-turonian upper Sarvak Formation, southwestern Iran. Geol Soc Lond Spec Publ, 330(1): 253–272

Hajikazemi E, Al-Aasm I S, Coniglio M (2012). Chemo stratigraphy of Cenomanian-Turonian carbonates of the Sarvak Formation, southern Iran. J Pet Geol, 35(2): 187–205

Haq B U, Al-Qahtani A M (2005). Phanerozoic cycles of sea-level change on the Arabian Platform. GeoArabia, 10(2): 127–160

Hollis C (2011). Diagenetic controls on reservoir properties of carbonate successions within the Albian–Turonian of the Arabian Plate. Petrol Geosci, 17(3): 223–241

Hopkins J C (1999). Characterization of reservoir lithologies within sub-unconformity pools: Pekisko Formation, Medicine River Field, Alberta, Canada. AAPG Bull, 83: 1855–1870

James N P, Choquette P W (1988). Paleokarst. New York: Springer-Verlag

Jia L Q, Cai C F, Jiang L, Zhang K, Li H X, Zhang W (2016). Petrological and geochemical constraints on diagenesis and deep burial dissolution of the Ordovician carbonate reservoirs in the Tazhong area, Tarim Basin, NW China. Mar Pet Geol, 78: 271–290

Jin M D, Zeng W, Tan X C, Li L, Li Z Y, Luo B, Zhang J L, Liu J W (2014). Characteristics and controlling factors of beach-controlled karst reservoirs in Cambrian Longwangmiao Formation, Moxi-Gaoshiti area, Sichuan Basin, NW China. Pet Explor Dev, 41(6): 712–723

Jolley S J, Fisher Q J, Ainworth R B (2010). Reservoir compartmentalization: an introduction. In: Jolley S J, Fisher Q J, Ainworth R B, Vrolijk P J, Delisle S, eds., Reservoir Compartmentalization, 347. Geological Society, 362: 1–8

Liu H, Tan X C, Li L, Ding X, Cao J, Yang G, Ma T (2019). Eogenetic karst in interbedded carbonates and evaporites and its impact on hydrocarbon reservoir: a new case from Middle Triassic Leikoupo

Formation in Sichuan Basin, southwest China. J Earth Sci, 30(5): 908–923

Liu H Y, Tian Z Y, Liu B, Guo R, Yang D, Deng Y, Yu Y C, Shi K B (2018). Pore types, origins and control on reservoir heterogeneity of carbonate rocks in Middle Cretaceous Mishrif Formation of the west Qurna Oilfield, Iraq. J Petrol Sci Eng, 171: 1338–1349

Lousk R (1999). Paleocave carbonate reservoirs; origins, burial-depth modifications, spatial complexity, and reservoir implications. AAPG Bull, 83: 1795–1834

Luo B, Tan X C, Li L, Liu H, Xia J W, Du B Q, Liu X G, Mou X H (2010). Discovery and geologic significance of paleokarst unconformity between Changxing Formation and Feixianguan Formation in Shunan area of Sichuan Basin. Acta Petrol Sin, 31: 408–414

Machel H G, Lonnee J (2002). Hydrothermal dolomite-a product of poor definition and imagination. Sediment Geol, 152(3-4): 163–171

Mahdi T A, Aqrawi A A M, Horbury A D, Sherwani G H (2013). Sedimentological characterization of the mid-Cretaceous Mishrif reservoir in southern Mesopotamian Basin, Iraq. GeoArabia, 18: 139–174

Mahdi T A, Aqrawi A A M (2014). Sequence stratigraphic analysis of the mid-cretaceous Mishrif formation, southern mesopotamian basin, Iraq. J Pet Geol, 37(3): 287–312

de Periere M D, Durlet C, Vennin E, Caline B, Boichard R, Meyer A (2017). Influence of a major exposure surface on the development of microporous micritic limestones-example of the upper Mishrif Formation (Cenomanian) of the Middle East. Sediment Geol, 353: 96–113

Mehmandosti E A, Adabi M H, Woods A D (2013). Microfacies and geochemistry of the Middle Cretaceous Sarvak Formation in Zagros Basin, Izeh Zone, SW Iran. Sediment Geol, 293: 9–20

Moore C H, Wade W J (2013). Carbonate reservoirs: porosity and diagenesis in a sequence stratigraphic framework. Developments in Sedimentology, Elsevier.

Palmer M R, Edmond J M (1989). The strontium isotope budget of the modern ocean. Earth Planet Sci Lett, 92(1): 11–26

Pitman J K, Steinhour D, Lewan M D (2004). Petroleum generation and migration in the Mesopotamian Basin and Zagros Fold Belt in Iraq: results from a basin-modeling study. GeoArabia, 9(4): 41–72

Qiang Z T (1998). Geology of Carbonate Reservoir. China: Beijing, University of Petroleum Press (in Chinese).

Rahimpour-Bonab H, Mehrabi H, Navidtalab A, Omidvar M, Enayati-Bidgoli A, Sonei R, Sajjadi F, Amiri-Bakhtyar H, Arzani N, Izadi-Mazidi E (2013). Palaeoexposure surfaces in cenomanianesantonian carbonate reservoirs in the dezful embayment, SW Iran. J Pet Geol, 36(4): 335–362

Rahimpour-Bonab H, Mehrabi H, Enayati-Bidgoli A H, Omidvar M (2012). Coupled imprints of tropical climate and recurring emergence on reservoir evolution of a mid Cretaceous carbonate ramp, Zagros Basin, southwest Iran. Cretac Res, 37: 15–34

Roberts J, Turchyn A V, Wignall P B, Newton R J, Vane C H (2018). Disentangling diagenesis from the rock record: an example from the Permo-Triassic Wordie Creek Formation, East Greenland. Geochem Geophys Geosyst, 19(1): 99–113

Sadooni F N (2005). The nature and origin of upper cretaceous basin-margin rudist buildups of the mesopotamian basin, Southern Iraq, with consideration of possible hydrocarbon stratigraphic entrapment. Cretac Res, 26(2): 213–224

Scholle P A, Ulmer-Scholle D S A (2003). A color guide to the petrography of carbonate rocks: grains, textures, porosity, diagenesis. AAPG Mem, 77

Taylor A S, Lasaga A C (1999). The role of basalt weathering in the Sr isotope budget of the oceans. Chem Geol, 161(1–3): 199–214

Veizer J, Ala D, Azmy K, Bruckschen P, Buhl D, Bruhn F, Carden G A F, Diener A, Ebneth S, Godderis Y, Jasper T, Korte C, Pawellek F, Podlaha O G, Strauss H (1999). $^{87}Sr/^{86}Sr$, $\delta^{13}C$ and $\delta^{18}O$ evolution of Phanerozoic seawater. Chem Geol, 161(1–3): 59–88

Vincent B, Van Buchem F S P, Bulot L G, Jalali M, Swennen R, Hosseini A S, Baghbani D (2015). Depositional sequences, diagenesis and structural control of the Albian to Turonian carbonate platform systems in coastal Fars (SW Iran). Mar Pet Geol, 63: 46–67

Wang J, Guo R, Zhao L M, Li W K, Zhou W, Duan T X (2016). Geological features of grain bank reservoirs and the main controlling factors: a case study on Cretaceous Mishrif Formation, Halfaya oilfield, Iraq. Pet Explor Dev, 43(3): 404–415

Xiao D, Tan X, Xi A, Liu H, Shan S, Xia J, Cheng Y, Lian C (2016). An inland facies-controlled eogenetic karst of the carbonate reservoir in the Middle Permian Maokou Formation, southern Sichuan Basin, SW China. Mar Pet Geol, 72: 218–233

Xiao D (2017). Research on eogenetic karst of marine carbonate and its reservoir in the three major basins western China. Dissertation for Doctoral Degree. Chengdu: Southwest Petroleum University

Xiao D, Zhang B J, Tan X C, Liu H, Xie J R, Wang L C, Yang X, Ma T (2018). Discovery of a shoal-controlled karst dolomite reservoir in the Middle Permian Qixia Formation, northwestern Sichuan Basin, Southwest China. Energy Exploration & Exploitation, 36(4): 686–704 (in Chinese)

Xiao D, Tan X C, Zhang D F, He W, Li L, Shi Y H, Chen J P, Cao J (2019a). Discovery of syngenetic and eogenetic karsts in the Middle Ordovician gypsumbearing dolomites of the eastern Ordos Basin (central China) and their heterogeneous impact on reservoir quality. Mar Pet Geol, 99: 190–207

Xiao D, Tan X C, Fan L Y, Zhang D F, Nie W C, Niu T, Cao J (2019b). Reconstructing large-scale karst paleogeomorphology at the top of the Ordovician in the Ordos Basin, China: control on natural gas accumulation and paleogeographic implications. Energy Sci Eng, 7 (6): 3234–3254

Xiong Y, Tan X C, Zuo Z F, Zou G L, Liu M J, Liu Y, Liu L, Xiao D, Zhang J (2019). Middle Ordovician multi-stage penecontemporaneous karstification in north China: implications for reservoir genesis and sea level fluctuations, 183: 1–14

Yu Y C, Sun L D, Song X M, Guo R, Gao X J, Lin M J, Yi L P, Han H Y, Li F F, Liu H Y (2018). Sedimentary diagenesis of rudist shoal and its control on reservoirs: a case study of Cretaceous Mishrif Formation, H Oilfield, Iraq. Pet Explor Dev, 45(6): 1075–1087

Zhong Y, Tan X C, Zhao L M, Guo R, Li F, Jin Z M, Chen Y T, Xiao D (2019). Identification of facies-controlled eogenetic karstification in the Upper Cretaceous of the Halfaya oilfield and its impact on reservoir capacity. Geol J, 54(1): 450–465